# Coherent Radar Processing in Sea Clutter Environments, Part 1: Modelling and Partially Adaptive STAP Performance

**MICHAEL KENNETH McDONALD**
DRDC Ottawa
Ottawa, Canada

**DELPHINE CERUTTI-MAORI,** Senior Member, IEEE
Fraunhofer Institute for High Frequency Physics and Radar
Techniques (FHR)
Wachtberg, Germany

Performance of space–time adaptive processing (STAP) with adaptive matched filter detection for maritime surveillance is assessed using simulated maritime surface targets embedded in real radar sea clutter data and compared with conventional pulse-Doppler processing. Pre-Doppler and post-Doppler suboptimal STAP are examined, with pulse repetition interval (PRI)-staggered post-Doppler shown to provide best overall detection and constant false alarm rate performance. A two-component clutter model fit is used to explain variations of clutter characteristics and detector performance with Doppler frequency.

## I. INTRODUCTION

Wide area surveillance of maritime targets from airborne platforms has traditionally employed noncoherent, high bandwidth, i.e., fine range resolution and single-channel radar systems operating from low-altitude aircraft with grazing angles of less than a few degrees. The current plans of many countries to migrate the maritime surveillance activity to high-altitude platforms, such as high-altitude long endurance (HALE) and middle-altitude long endurance (MALE) unmanned aerial vehicles (UAVs) will result in steeper look-down geometries with associated high grazing angles (HGAs). Because even medium grazing angles of 25° can lead to increases in sea clutter cross-sections of 10–15 dB in comparison with low-grazing-angle geometries, the noncoherent detection performance is significantly degraded [1].

Noncoherent detection corresponds to the linear or square-law detection of radar echo pulses and results in the loss of phase or Doppler information. Typically, the noncoherent outputs are summed across a specified number of pulses to improve the resulting signal-to-clutter-plus-noise ratio (SCNR). A review of the details of noncoherent techniques is beyond the purview of this paper; refer to Skolnik [2] and Ward et al. [1] for a comprehensive introduction. One promising approach with the potential to help mitigate HGA performance degradation is the application of coherent processing techniques. This paper examines the use of both single- and multiaperture antenna systems, which allow temporal and spatial–temporal coherent processing, respectively. Single-channel coherent detection has a long history of application for the surveillance of air targets, while space–time adaptive processing (STAP) has been employed more recently for ground-moving target indication (GMTI). The success of GMTI processing results from the ability to spatially and temporally separate the signature of moving targets from stationary ground clutter. The transition of GMTI processing strategies to maritime surveillance is complicated by the dynamic motion of the sea surface, which results in sea clutter radar echo returns with broad and rapidly varying spectral content.

This paper is the first in a two-part series examining the issues surrounding the application of coherent processing techniques to maritime radar surveillance problems. The work expands significantly on earlier investigations by carefully examining STAP performance versus Doppler frequency for a range of SCNRs at operational probabilities of false alarm [3–6]. The goal of the two-part series is to quantitatively evaluate the constant false alarm rate (CFAR) and detection performance of current adaptive processing strategies and detector structures when applied to maritime radar surveillance from airborne platforms. The relative performance gains between simpler, less costly single-channel systems and elaborate multiaperture systems are quantified with

TABLE I
Acronym List

| 2D | Two dimensional |
|---|---|
| ABPD | Adjacent bin post-Doppler |
| AMF | Adaptive matched filter |
| ANMF | Adaptive normalised matched filter |
| APDF | Amplitude probability density function |
| AR | Autoregressive |
| CA | Cell averaging |
| CCDF | Complementary cumulative density function |
| CFAR | Constant false alarm rate |
| CN | Circular normal |
| CNR | Clutter-to-noise ratio |
| CPI | Coherent processing interval |
| CUT | Cell under test |
| EM | Electromagnetic |
| FFT | Fast Fourier transform |
| FS | Fast scattering |
| GLRT | Generalised likelihood ratio test |
| GMTI | Ground-moving target indication |
| HALE | High-altitude long endurance |
| HGA | High grazing angle |
| ICM | Internal clutter motion |
| KpK | K plus K |
| KpR | K plus Rayleigh |
| MALE | Middle-altitude long endurance |
| ML | Maximum likelihood |
| PAMIR | Phased-array multifunctional imaging radar |
| PD | Probability of detection |
| pdf | Probability density function |
| PFA | Probability of false alarm |
| PreD | Pre-Doppler |
| PSPD | PRI-staggered post-Doppler |
| ROC | Receiver operating characteristics |
| SCM | Sample covariance matrix |
| SCNR | Signal-to-clutter-plus-noise ratio |
| SINR | Signal-to-interference-plus-noise ratio |
| SIRP | Spherically invariant random process |
| SNR | Signal-to-noise ratio |
| STAP | Space–time adaptive processing |
| SW0 | Swerling 0 |
| SW1 | Swerling 1 |
| UAV | Unmanned aerial vehicle |



Fig. 1. Flight geometries in east–north–up coordinate system. Wind direction and swell direction are indicated by black and red arrows, respectively. Colour codes pointing angle of antenna.

significant effort devoted to developing an understanding of why departures from ideal performance occur. In this first paper, the spectral and statistical properties of a real maritime data set collected using the Fraunhofer Institute for High Frequency Physics and Radar Techniques (FHR) phased-array multifunctional imaging radar (PAMIR) are carefully examined and modelled. The data set is then processed using several popular, suboptimal, partially adaptive STAP techniques that were originally developed for the GMTI problem. Departures of performance from those commonly observed with land clutter are noted and explained based on the aforementioned clutter modelling. The second paper examines the application of the adaptive normalised matched filter (ANMF), which is frequently advocated as a formulation well tailored to sea clutter environments. A useful survey of underlying clutter models and detector structures is presented by Gini and Farina [7]. Departures from ideal performance are noted
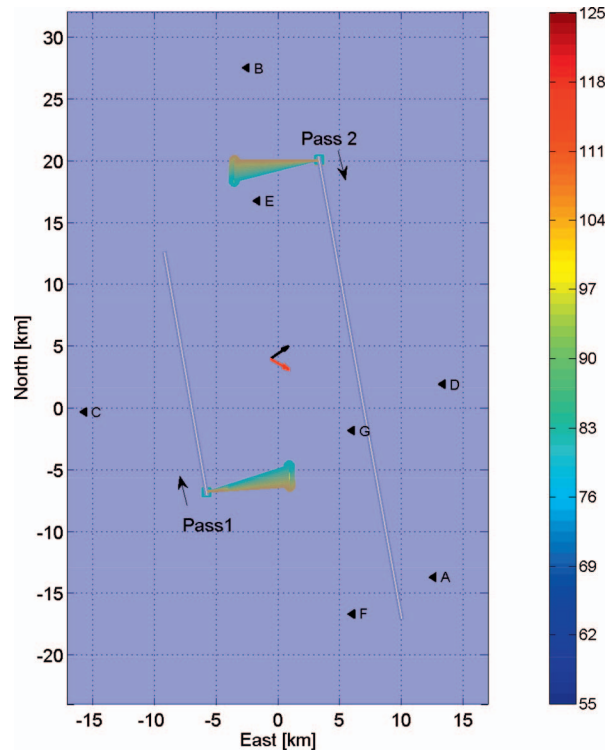
and explained via the clutter model. Proposed modifications to the detector structure are examined and tested.

A list of the acronyms used in this paper is provided in Table I.

## II. DATA COLLECTION

The data underlying the analysis in this paper was acquired using the FHR PAMIR system operating in a scan-moving target indication mode in a side-looking configuration [6, 8]. During the collection trial, the radar platform flew at an altitude of 2500 m (8200 feet) with a velocity of 100 m/s. The antenna grazing angle was approximately 20°. Two data collection passes (Fig. 1) were undertaken, with look directions corresponding to approximately downwind (pass 1) and upwind (pass 2) geometries, i.e., wind is blowing away from and towards the radar antenna pointing direction, respectively. The trial took place in the North Sea between Helgoland and Wilhelmshaven in Germany in December 2009. The PAMIR system employed a three-channel, 80-cm, V-V polarised phased-array antenna. Key operating parameters and collection geometry details are provided in Table II. Data are collected using two transmit frequencies; both data sets are used to maximise the total number of measurements. All corresponding Doppler frequencies are calculated per the applicable transmit frequency. During transmit, the three antenna apertures are coherently

TABLE II
Operating Parameters and Collection Geometry for PAMIR Data Set

| | |
|---|---|
| Mean range from aircraft to target | 7.3 km |
| Viewing geometry | Side looking with respect to aircraft motion |
| Aircraft altitude | 2500 m (8200′) |
| Grazing angle | 20° |
| Platform velocity | 100 m/s |
| Range resolution | 7.5 m |
| Transmit frequency | 9.09 and 9.50 GHz |
| Antenna azimuth | 80 cm |
| Number of channels | 3 |
| Antenna phase centre separation | 26.6 cm |
| Antenna transmit and receive polarisation | V-V |
| CPI | 42.6 ms |
| Effective pulse repetition frequency | 3 kHz |
| Centre point of data take | (53.98° N, 7.91° E) |

combined to create a single effective transmitting aperture. Environmental conditions are provided in Table III and were derived at the locations indicated in Fig. 1 from wind measurement devices (A–C), wave buoys (D), and the German forecast (E–G). Sea conditions were moderate, with a reported swell height of 0.9–1.5 m and a wind sea wave height of 0.4–0.5 m.

Cooperative maritime targets were not fielded as part of the trial, and artificial Swerling 0 (SW0) targets of specified radial velocity are inserted into the real data to permit assessment of detection performance. Real-world detection performance against actual targets would be expected to be degraded because of effects such as target incoherence and straddling losses, but the following analysis provides a useful baseline for comparing processing techniques and eliminates issues surrounding variations of real target radar cross-sections with time and viewing angle. Limited testing was also performed using a Swerling 1 (SW1) assumption for the variation of target amplitudes between coherent processing intervals (CPIs). While the use of a SW1 target assumption was seen to slightly flatten the receiver operating characteristics (ROC) curves in comparison with the SW0 curves presented in Section VI, it does not fundamentally alter the observations about relative performance. The SW1 results are not further discussed in this paper for conciseness.

## III. SEA CLUTTER CHARACTERISTICS

The sea surface is a highly dynamic environment that generates a complex Doppler radar signature dependent on a variety of external factors, such as wind speed, fetch, ocean currents, and sea depth, as well as radar-dependent parameters such as transmitter frequency, radar waveforms, and viewing geometries. The complexity of the sea surface hydrodynamics results in a difficult electromagnetic (EM) modelling problem, and the topic remains an active area of research. Given the challenges associated with direct EM modelling, it is common for detection strategies to rely extensively on stochastic clutter

models developed primarily from empirical observations. It is helpful to review some key observations of past investigations, because they provide a foundation for the discussion presented in this paper.

Early modelling of sea clutter returns for low-resolution radars successfully employed Rayleigh amplitude or exponential power statistics to describe the linear or square-law amplitude detection statistics, respectively. See, for instance, Skolnik [2] and references therein. As the need arose to detect targets with ever-smaller radar cross-sections, higher-resolution (or higher-bandwidth) radars were developed with a goal of shrinking the competing clutter patch so as to improve the SCNR. Although an improvement in SCNR was observed for high-resolution designs, a concurrent increase of high-amplitude events was observed in comparison with Rayleigh predictions. Clutter displaying this behaviour is commonly called spiky. A range of amplitude probability density functions (APDFs) have been empirically fitted to these observed results, with popular examples including the Weibull and lognormal distributions, as well as the more general class of compound-Gaussian distributions. An excellent review of the topic is provided in Ward et al. [1]. Different data sets are often best modelled by different distributions, a result that underscores that there is typically no underlying physical argument to support the use of a particular APDF. Compound-Gaussian distributions, and in particular the specific example of the K distribution, are the exceptions to this rule in that they admit a physical interpretation with a partial correspondence to some elements of the observed ocean structure. The mathematical form of the compound-Gaussian distribution is as follows:

$$p(E) = \int_0^\infty e^{\frac{-E^2}{x}} p_x(x)\mathrm{d}x, \qquad (1)$$

where $E$ is the clutter amplitude, $x$ is the underlying local clutter power or texture, and $p_x$ is the corresponding probability density function (pdf). For the K distribution, the underlying texture is modelled as a correlated gamma variate modulating a complex circular normal (CN) speckle component. The texture and speckle components are qualitatively associated with the effects of the gravity wave and capillary wave structures, respectively, on the sea surface [9, 10].

While stochastic behaviour of compound-Gaussian formulations is consistent with some aspects of the empirical results, these formulations do not fully explain all observed features and it is necessary to introduce additional clutter mechanisms. To aid in the discussion of these additional underlying mechanisms, it useful to distinguish between the so-called fast scattering (FS) and slow scattering responses of the sea clutter spectrum. The slow scattering response is primarily associated with resonant Bragg scattering from the capillary wave structure on the sea surface. The relatively low Doppler frequencies of the slow scattering response coincide with the phase velocity of capillary waves, with values on the

TABLE III
Environmental Parameters Measured at Several Local Measurement Stations during Trial Collection Period

| Time (UTC) | Wind direction | Wind speed | Swell direction | Swell wave height | Swell period | Wind sea direction | Wind sea wave height | Wind sea period | Identifier |
|---|---|---|---|---|---|---|---|---|---|
| 17:00 | 230° | 5.1 m/s | — | — | — | — | — | — | A |
| 18:00 | 240° | 6.2 m/s | — | — | — | — | — | — | |
| 17:00 | 260° | 5.1 m/s | — | — | — | — | — | — | B |
| 18:00 | 250° | 5.1 m/s | — | — | — | — | — | — | |
| 17:00 | 210° | 2.7 m/s | — | — | — | — | — | — | C |
| 18:00 | 230° | 2.1 m/s | — | — | — | — | — | — | |
| 16:54 | — | — | 296° | 1.0 m | — | — | — | 4.2 s | |
| 16:24 | — | — | 297° | 1.0 m | 8.3 s | — | — | 4.3 s | D |
| 17:54 | — | — | 289° | 0.9 m | 11.1 s | — | — | 4.3 s | |
| 18:00 | 240° | 5.6 m/s | 300° | 1.5 m | 11 s | 240° | 0.5 m | 3 s | E |
| 18:00 | 230° | 5.6 m/s | 310° | 1.1 m | 11 s | 230° | 0.4 m | 2 s | F |
| 18:00 | 230° | 5.1 m/s | 300° | 1.3 m | 11 s | 230° | 0.5 m | 3 s | G |

order of tens of hertz for X-band systems. Capillary waves propagate predominantly in the same direction as the wind that generates them. The broad features of the Bragg scattering spectrum have been successfully captured through EM modelling employing composite or two-scale models, in which the Bragg scattering response is modulated by the action of sea surface gravity waves; see, for instance, [11, 12]. The Bragg scattering response typically dominates in data collected using a V-V polarised radar system. In contrast, data collected using an H-H polarised system can be heavily affected by FS mechanisms that exhibit higher Doppler frequencies. Walker [13, 14] associated the generation of the FS response with the presence of two separate mechanisms, corresponding to wave breaking and reflections from the fronts of wave before breaking. The latter mechanism is called burst scattering. Per these previous studies, burst scattering is expected to be mostly absent for low-grazing-angle (i.e., less than a few degrees), downwind viewing configurations because of obscuration effects. FS events have been shown to have effective velocities on the order of metres per second corresponding to Doppler frequencies on the orders of hundreds of hertz for the X-band system employed in this study. Studies using wave tanks and ground-based measurements of the open sea have shown that the presence of FS and slow scattering frequently leads to a bimodal mean Doppler spectrum [13–15].

The physical interpretation of the K distribution as a modulation of the Bragg scattering cross-section by a linear superposition of underlying gravity waves is not inclusive of FS mechanisms described earlier. Furthermore, fits of the K distribution to real data frequently fail to capture the level of enhancement, or spikiness, observed in the high-amplitude tail of the APDFs. The class A-plus-K or KA model represents an attempt to capture the statistical impact of these additional mechanisms by incorporating discrete spike components into the K distribution. These discrete spike events

have been qualitatively identified as arising from FS mechanisms [16, 17].

The statistical APDFs used in the development and analysis of noncoherent detector structures do not incorporate information with regards to the sea clutter spectrum. To address this shortcoming, spherically invariant random process (SIRP) has been suggested as a tractable statistical characterisation of the complex envelope of the sea clutter radar echo returns. The SIRP is a complex analogue to the compound-Gaussian formulations described earlier; the popular K distribution represents an admissible solution for an envelope-detected SIRP. Implicit in the definition of the SIRP is the assumption that the underlying power (or texture) remains constant across the CPI corresponding to the measurement vector and that the relative spectral content remains constant between CPIs. This implies that a common power scaling factor affects all spectral components of the underlying clutter equally, i.e., the underlying power spectrum from different realisations of the measurement vector is identical up to a common scalar in the absence of receiver noise. In statistical terms, this means that ensemble samples drawn from different frequency bins have identical shape parameters and only differ in their scale values. This assumption would appear to be inconsistent with the preceding discussion on the existence of independent physical mechanisms, which give rise to independently varying fast and slow clutter spectrum components. The potential for significant nonhomogeneity of clutter characteristics in both space and time because of the presence of FS events has been previously discussed by McDonald and Cerutti-Maori [5] and McDonald et al. [6] for H-H clutter. For the V-V polarised PAMIR data, the effect of fast scatterers is less pronounced, although not wholly absent, as discussed in Section IV. The mathematical formulation of the SIRP and the impact of SIRP statistics on detector development and performance are examined in depth in the companion paper in this series [18].
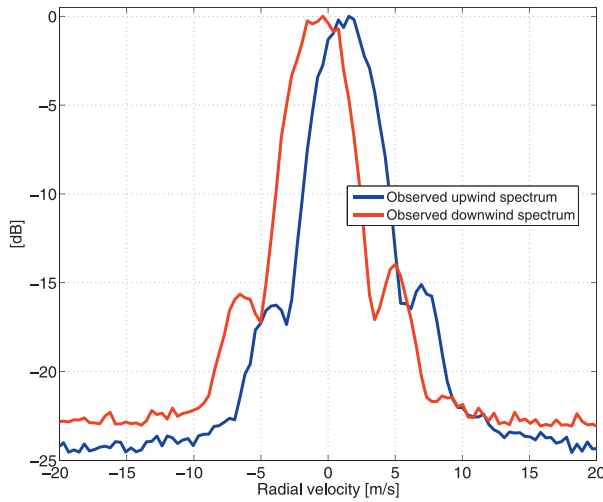
Fig. 2.   Measured Doppler spectrum from PAMIR data for upwind and downwind directions. Each spectrum is normalised with respect to its peak power. Upwind CNR is observed to be larger than downwind CNR.



Fig. 3.   Space–time characteristics. Top left: Antenna pattern versus steering angle. Top right: 2D angle versus Doppler spectral pattern. Bottom left: Comparison of pure Bragg versus Bragg + FS inherent spectra. Bottom right: Projection of 2D angle versus Doppler pattern onto Doppler axis.

## IV.   CHARACTERISATION OF PAMIR DATA

### A.   Spectral Characteristics

Fig. 2 presents the mean Doppler spectrum observed for the PAMIR data for the upwind and downwind viewing directions. Throughout this paper, the convention is adopted that targets or clutter approaching the radar have positive velocities (and positive Doppler frequency shifts) while those moving away from the radar have negative velocities (and negative Doppler frequency shifts). The observed behaviour is broadly consistent with expectations of the Doppler spectral peak being shifted to positive and negative Doppler frequencies for the upwind and downwind directions, respectively. The peaks are associated with the capillary wave velocities responsible for generating the Bragg response. Both curves have been normalised to 0 dB at the peak. This results in the observed noise floor appearing to be lower for the upwind direction even though the receiver noise power is constant. This apparent shift is indicative of the stronger clutter power return from the upwind direction. A stronger upwind clutter return is also consistent with past observations of the look direction dependency of sea clutter radar cross-sections [1].

It is well known from the development of airborne GMTI systems that the motion of the aircraft, combined with the antenna azimuth beamwidth, induces Doppler broadening of the land clutter spectrum, which is most pronounced for broadside viewing geometries [19]. A similar effect occurs for sea clutter and is evident in the spectral responses of Fig. 2. To better illustrate this effect, Fig. 3 presents a simulated sea clutter Doppler response corresponding to a downwind viewing geometry. The top right panel corresponds to the two-dimensional (2D) steering angle versus Doppler frequency response that would be observed with the PAMIR antenna configuration when all three antenna apertures transmit coherently at a
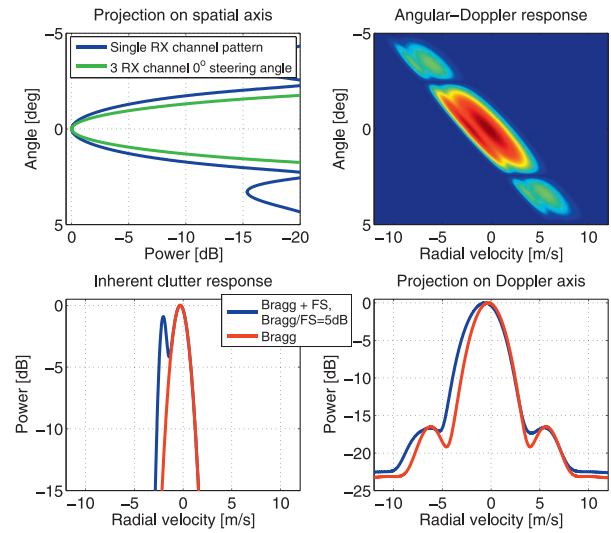
steered angle of $0°$ (corresponding to the side-looking direction, i.e., the antenna pointing angle of $90°$ with respect to aircraft velocity vector) and only one aperture is assumed used for receiving. Very high Doppler resolution is assumed, i.e., minimal windowing effects. The clutter response is assumed to result from a combination of Bragg and FS (Bragg + FS) clutter mechanisms, and the blue curve in the bottom left panel corresponds to the inherent spectrum. The inherent spectrum is defined as the spectrum that would be observed if Doppler broadening was not present, i.e., the stationary platform. For comparison, the red curve corresponds to a pure Bragg clutter spectrum. The choice of parameters values for the Bragg and FS components is discussed further in Section IV.B. The blue curve in the bottom right panel of the figure corresponds to the Doppler-broadened spectral response of the simulated Bragg and FS components that would be available for further processing in a system without spatial diversity, i.e., if only the Doppler frequency could be measured. The red curve displays the corresponding Doppler-broadened Bragg clutter response. These curves are derived by projection of the 2D response onto the Doppler axis. The significant effect of Doppler broadening is evident from comparison of the bottom panels, where it is observed that the 3-dB Doppler velocity bandwidths of the inherent and broadened Bragg + FS spectra are approximately 3 and 3.7 m/s, respectively, from the left and right panels. The broadening effect is even more pronounced for the pure Bragg response, which shows a greater proportional change in bandwidth between the inherent and the Doppler-broadened spectrum. The top left panel presents the analogous projection onto the spatial axis and corresponds to the antenna beam pattern. Two curves are displayed: the blue curve corresponds to the use of a single subaperture on receive and the green curve
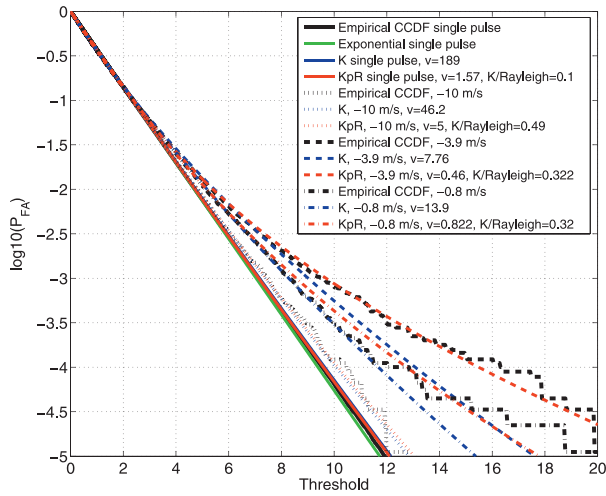
Fig. 4. CCDF curves for PAMIR data for single-pulse and selected frequency bins after application of FFT. Downwind viewing geometry.



Fig. 5. CCDF curves for PAMIR data for single-pulse and selected frequency bins after application of FFT. Upwind viewing geometry.

corresponds to the coherent addition of all three apertures on receive for a steered angle of $0°$.

Some key features are as follows. While the inherent Bragg + FS spectrum is bimodal in character, the bimodality is not easily observable in the broadened spectrum. As such, it is difficult to identify the presence of separate clutter mechanisms from observations of the broadened spectra alone. The shifted and broadened Bragg + FS spectrum could easily be misinterpreted as arising from a slightly broadened Bragg spectrum centred at different Doppler frequencies because of, say, an underlying ocean current. The details of the observed spectral response are discussed in more detail in Section IV.B. Similar characteristics are observed for the upwind viewing direction but are not discussed further for conciseness.

B. Statistical Characterisation of Data

To better appreciate the implications of moving from noncoherent to coherent processing approaches, we compare the statistical characteristics of noncoherent (envelope detected) data with coherently processed data. Figs. 4 and 5 present empirically derived curves of the complementary cumulative density functions (CCDFs) or, equivalently, the probability of false alarm (PFA) versus threshold, for the PAMIR downwind and upwind data sets, respectively, after coherent summation of the three-channel data, i.e., after application of a $0°$ steering vector. CCDFs are presented for single-pulse (no pulse to pulse integration) noncoherent values across the full set of range cells and for a range of selected Doppler bins. Doppler bin data are extracted by taking the fast Fourier transform (FFT) of measurement vectors corresponding to CPIs of 64 pulses. For both single-pulse and Doppler analysis, the data are normalised to remove large-scale underlying power fluctuations using a cell averaging (CA) approach in which each cell under test (CUT) is divided by the mean power estimate derived from 128 range cells
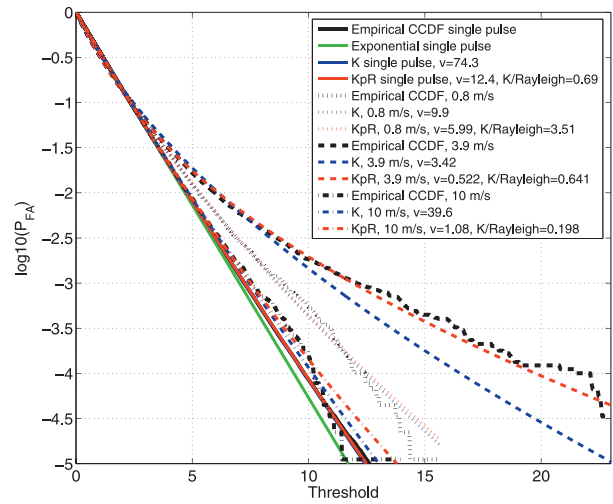
distributed equally on each side of the CUT, with 3 guard cells per side. The background sample range corresponds to approximately 770 m and reduces the variations because of range spreading and antenna elevation gain pattern. For single-pulse curves, the normalisation is applied pulse by pulse; for the Doppler analysis, the normalisation is calculated for each Doppler frequency bin individually. This approach of taking the FFT and normalising for mean power is equivalent to the single-channel processing used in this study and is subsequently called pulse-Doppler processing.

In addition to the empirically derived CCDF curves, moment-based fits to the underlying data for exponential, K-distributed, and K-plus-Rayleigh (KpR)–distributed pdfs are presented in Figs. 4 and 5. For compactness, only a small subset of the Doppler bins is presented so as to highlight the salient features. In addition, the exponential fit is only presented for the single bin statistics, because the exponential fits for the coherent Doppler bins are similar and provide no additional useful information. The KpR distribution is mathematically equivalent to the K-plus-receiver noise previously presented by Watts [20] but with the noise component presumed to be composed of both receiver noise and returns from a Rayleigh-distributed Bragg component. The motivation for using the KpR fit arose from recent observations by members of the North Atlantic Treaty Organization (NATO) Sensors and Electronic Technology (SET) 185 panel that a number of different HGA CCDFs were frequently well fit by this distribution. Rosenberg et al. [21] have since published results for one of these data sets. The shape parameter of the K component for the K and KpR distributions is designated by $\nu$ and is calculated using the moment-based method outlined in Ward et al. [1]. Examination of the single-pulse CCDF curves indicates that the noncoherent clutter statistics are well modelled by an exponential APDF to at least the $10^{-5}$ PFA level. As such, the CFAR performance of a

noncoherent detector structure developed per an assumption of exponentially distributed clutter should be well behaved against this data set. Furthermore, because an exponential pdf is fully specified by a scale parameter based on a first-order moment, the sample support requirement is relatively small and the adaptive estimation should be reasonably simple to implement, e.g., CA-CFAR detector. The preceding characteristics are consistent with expectations for the V-V polarised PAMIR data, which has a low sea state and a relatively low total clutter-to-noise ratio (CNR) of approximately 10 dB. V-V tends to be less spiky than H-H data.

In contrast, the −10, −3.9, and −0.8 m/s pulse-Doppler curves of Fig. 4 exhibit increasingly spiky CCDF curves, with a similar behaviour noted for the complementary positive velocities of the upwind data in Fig. 5. The spikiest results are associated with velocities deeply embedded in the clutter spectrum, a condition commonly called endoclutter. Velocities for which little clutter is present are said to be exoclutter. For instance, the ±10 m/s curves are predominantly exoclutter and show only slightly elevated tails with respect to exponential predictions, whereas the ±3.9 and ±0.8 m/s curves are unambiguously endoclutter and exhibit pronounced tails. This trend is anticipated, because the CNR increases as one approaches the peak of the clutter spectrum, i.e., maximum spikiness coinciding with spectral peaks, due to effects of the antenna azimuth gain pattern. To further examine the preceding behaviour, the effective shape parameter and mean clutter spectrum are plotted versus Doppler velocity in Figs. 6 and 7 for the downwind and upwind direction, respectively. The effective shape parameter was defined by Watts [20] as tool for dealing with interference composed of K-distributed sea clutter and Rayleigh noise. For both downwind and upwind directions, the corresponding velocity of the spikiest, or smallest shape parameter, values does not coincide with the peak of the power clutter spectrum. In particular, the spikiest clutter is approximately centred at the −3.9 and +3.9 m/s Doppler velocity bins for the downwind and upwind results, while the peak spectral powers occur around −0.8 and 1.5 m/s, respectively. This observation is inconsistent with an assumption of a SIRP model for the sea clutter. The general pattern of variation of the shape parameter with Doppler is qualitatively similar to that observed by Ritchie et al. [22] for X-band data collected using different radar at a different location and time.

The best fits for the −3.9 and 3.9 m/s Doppler velocities of Figs. 4 and 5, respectively, are achieved with a KpR distribution in which the Rayleigh power component exceeds the expected receiver noise power. While this observation is suggestive of a two-component clutter model consisting of a spiky clutter component and a Rayleigh clutter component, one cannot definitively deduce the presence of separate clutter mechanisms based solely on this result. It is axiomatic that reasonable candidate distributions with more degrees of freedom will typically achieve better fit to data than distributions with
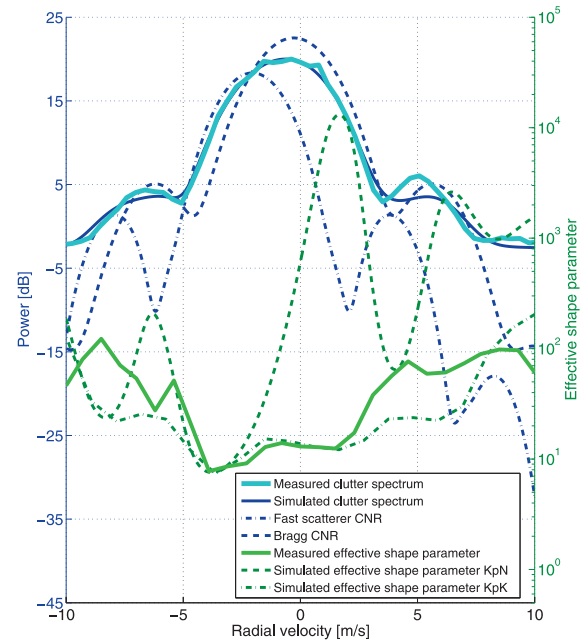


Fig. 6. Comparison of measured effective shape parameter and measured spectrum to fitted spectra and estimated effective shape parameters per KpR and KpK models for downwind viewing geometry. Peaks of measured and simulated total clutter power spectra curves were arbitrarily set to 20 dB for clarity. Blue-shaded plot curves refer to spectral power fits (left y-axis), while green-shaded plot curves refers to effective shape parameter (right y-axis).
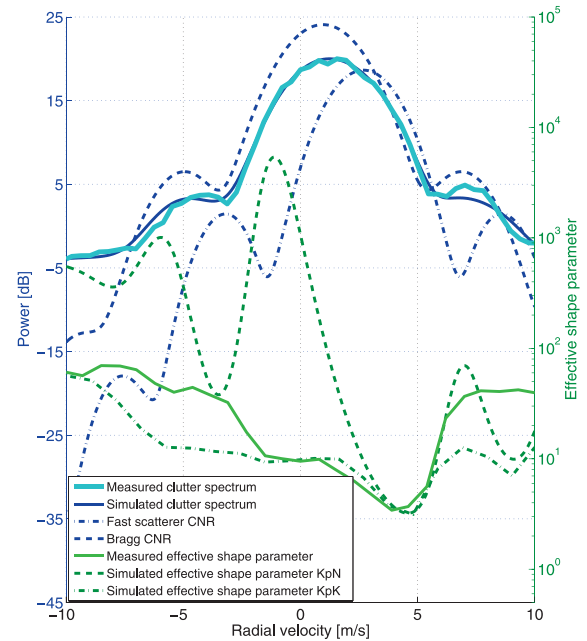


Fig. 7. Comparison of measured effective shape parameter and measured spectrum to fitted spectra and estimated effective shape parameters per KpR and KpK models for upwind viewing geometry. Peaks of measured and simulated total clutter power spectra curves were arbitrarily set to 20 dB for clarity. Blue-shaded plot curves refer to spectral power fits (left y-axis), while green-shaded plot curves refers to effective shape parameter (right y-axis).

fewer adjustable parameters, even though the former formulation may not represent the underlying physical clutter mechanisms. We further examine the validity of a two-component clutter model later. A final feature of note is that the fitted upwind CCDF for the 3.9 m/s Doppler velocity bin is significantly spikier than the corresponding −3.9 m/s downwind CCDF, a result consistent with the discussion of Section III, in which burst-scattering events are observed to be unlikely for downwind viewing geometries.

The increased spikiness of pulse-Doppler clutter statistics has important implications with regards to the implementation of coherent detection approaches. In particular, envelop-detected data that were well approximated by Rayleigh statistics now exhibit a frequency-dependent increase in spikiness under coherent processing. As discussed in Sections VI.A and VI.C, this frequency-dependent spikiness directly affects the detection performance and is problematic with regards to obtaining CFAR performance. The enhanced spikiness is observed despite the relatively moderate sea state conditions that prevailed during this trial.

To better understand the genesis of the observed behaviour, a simple two-component clutter model was fitted to the data that successfully predicts the endoclutter variation of both effective shape parameter and spectral power with Doppler frequency. The addition of the effective shape parameter as a fitted observable was found to significantly constrain the range of acceptable solutions. Furthermore, it was determined that modelling of the observed variation of spectral power and effective shape parameter with these types of spectral models required the presence of at least two independent clutter mechanisms. This contrasts with previous fits to broadened spectra using only spectral information, for which there is insufficient information to definitively determine whether the asymmetrical response arises because of independent clutter components [23]. The use of a shape parameter (a measurement-derived parameter) as a constraint was also shown to reduce the need for arbitrary constraints, such as a requirement for FS bandwidth to be larger than Bragg component, that were required to produce realistic fits under spectral-only approaches.

The statistical formulation of the first model investigated corresponds closely to the KpR formulation proposed by Ward and Tough [17]. The approach in this paper differs only in that K and Rayleigh component power ratios are seen to vary between frequency bins. Per Ward and Tough, the underlying clutter is presumed to be composed of a FS response that is K distributed and a Bragg response that is Rayleigh distributed [17]. In this paper, we further assume each component to have a simple Gaussian-shaped inherent spectrum. Based on these assumptions, the model of the inherent sea clutter then requires the specification of the spectral width and centre frequency of the two-component clutter spectra, the FS-to-Bragg power ratio, and the shape parameter of the FS statistics to be adjusted to obtain the best fit. All these

parameters are determined during the fitting process. The simulated spectrum and simulated KpR effective shape parameters are presented in Figs. 6 and 7 for comparison with empirical values. This representation clarifies the contribution of each component to a particular Doppler bin. The spectral response of each clutter component can be seen to have been significantly widened by Doppler spreading and is highly reminiscent of the azimuth antenna pattern. Although the fitted curves are not unique, extensive experimentation indicates that the uniquely asymmetrical shape of the effective shape parameter with respect to the spectral peak is only obtained when the two separate clutter responses are offset in Doppler velocity and possess different stochastic characteristics. More particularly, a high-velocity, spiky clutter component is required to reproduce the effective shape parameter minimums observed at −3.9 and 3.9 m/s for the downwind and upwind directions, respectively. During the fitting process, extra weight is given to obtaining a good spectral match across the main lobe, with larger departures from fit tolerated in the low clutter power sidelobes. It can been seen that the simulated and fitted Doppler spectra are closely matched down to at least 15 dB below the main lobe peak.

Although the KpR model successfully captures some key features, such as the overall spectrum and the minimum of the effective shape parameter curve, a close examination of the simulated effective shape parameter curve reveals several velocity bands in which the simulated effective shape parameter value is much larger than the measured effective shape parameter. Significant improvements in the fit across these regions can be achieved if the Bragg component is also assumed to be K distributed, i.e., assumed to have a finite shape parameter. The corresponding model is composed of two K-distributed components with different shape parameters and is called the K-plus-K (KpK) model. The KpR and KpK formulations do not represent mixture models; rather, they represent the pdfs that will result if independent variates from the two identified components are summed. Some potential mathematical formulations for a KpK distribution are discussed in the companion paper of this series. Because the definition of effective shape parameter per Watts [20] was based on an assumption of K plus exponential noise, there is no closed-form equation to determine the effective shape value that would result under a KpK model. As such, we determine the effective shape parameter that would be observed for any given KpK combination using Monte Carlo simulation.

The KpK effective shape parameter curves in Figs. 6 and 7 provide a closer match to empirical results, although there are discrepancies. In particular, the KpK results tend to underestimate the effective shape parameter in the velocity regions outside the main lobe of the observed clutter response. This mismatch highlights a shortcoming of the modelling approach. Fig. 8 presents spectra that would be observed per the fitted upwind parameters for two cases corresponding to an infinitely narrow frequency
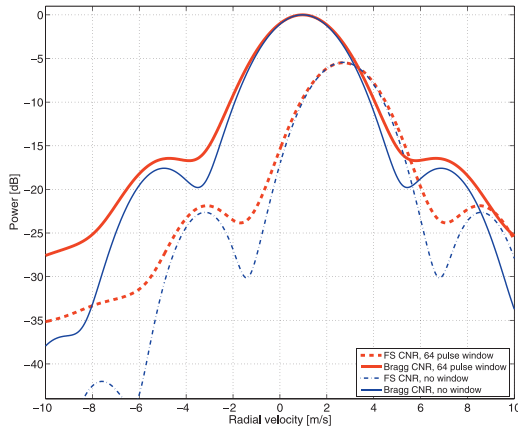
Fig. 8. Comparison of windowed and unwindowed fitted frequency spectra for upwind viewing geometry.

resolution (i.e., infinitely or, at least, very long CPI) and the 64-pulse CPI used in this study. It is observed that the most pronounced differences between the spectra coincide with the aforementioned regions of mismatch between modelled and measured effective shape parameters. In these velocity regions, the powers of the dominant clutter components of the windowed response are seen to be elevated with respect to high-resolution results. This well-known effect arises because of leakage of clutter power from the main clutter lobe into the high-velocity regions through sidelobes in the windowing function frequency response. Because the clutter signal from the main lobe and desired velocity regions are independent, their addition causes an increase in the effective shape parameter. In effect, the clutter response in these regions can be considered as arising from a four-component (or higher) clutter model composed of Bragg scattering and FS from the current velocity bin and the leakage signal from the main lobe. Because the calculation of the modelled effective shape parameter in this study only considers the ratio of the clutter power from the two independent components, it underestimates the measured effective shape parameter in these regions of large main lobe clutter leakage.

The tendency for the addition of independent clutter components to raise the effective shape parameter is also visible in the local maximums observed at $-1.5$ and $1.5$ m/s for the downwind and upwind cases, respectively, although these cases are not related to sidelobe leakage because of the windowing function.

Fitted parameters are listed in Table IV. An important observation from Figs. 6 and 7 and Table IV is that the minimum effective shape parameter does not coincide with the peak of the FS spectrum. The FS peak occurs at significantly slower velocities corresponding to $-2.0$ and $+2.6$ m/s for the downwind and upwind directions, respectively. The minimum effective shape parameter can be seen to coincide with the Doppler velocity at which the ratio of FS to Bragg component power is at maximum (although still well below the peak of either the FS and the Bragg power spectrum). Simulated effective shape

parameter results were less accurate for the upwind direction. Possible reasons for the greater discrepancies include departures from the assumptions of Gaussian spectral shape and two-component models. Experimentation with other spectral shapes, e.g., sinc versus Gaussian, indicates minimal sensitivity to variations in the shape of the main lobe because of the broadening effect of the convolution with the antenna azimuth beam pattern. It is possible that the presence of significant sidelobes in the inherent spectrum could have some effect. The validity of the two-component model remains an open question. Per Section III, three mechanisms for clutter generation have been identified, corresponding to Bragg, whitecap, and burst scattering, with burst scattering expected to be significant only for the upwind viewing geometry. Ward and Tough [17] previously associated the K component of the KpR model with whitecap scattering, which tends to have a broad frequency speckle-like response. In contrast, burst scattering is observed to be more coherent and is likely to have a poor correspondence to K-distributed clutter. The application of three-component model is discussed further in the companion paper to this series [18].

The preceding analysis raises important practical considerations in the development of coherent systems. The results of Figs. 6 and 7 were derived using an angular steering vector steered to $0°$ per the PAMIR characteristics of Table II. As discussed, the effective shape parameter depends on the ratio of the FS and Bragg-plus-receiver noise component powers. From Fig. 3, it is observed that these ratios are a function of position within the 2D angle versus frequency clutter spectrum pattern and, as such, the relationship between Doppler velocity and effective shape parameter is altered for different steered angles. In other words, the effective shape parameter is not just a function of Doppler frequency but also dependent on the steered angle. Furthermore, the amount of Doppler spreading depends on both the platform velocity and the squint angle. For scanning radars, these latter factors act as additional sources of variation in the clutter statistics, with implications for CFAR operation. This, in turn, could negatively affect detection performance if detection decision thresholds are inadvertently set too high.

In summary, several key concepts have been discussed:

1) Clutter backscatter characteristics can become significantly spikier when processed coherently.

2) Statistical properties are observed to depart from those predicted by a CN process or SIRP.

3) Statistics within individual Doppler bins can be well fit using a variety of pdfs, such as the KpR, but results are inconsistent with physical interpretations.

4) Physically consistent results are obtained through the use of multicomponent clutter models in which the fits are constrained to match the statistical and backscatter power behaviour across all Doppler bins.

TABLE IV
Fitting Parameters for Two-Component Model

| | FS velocity | FS width | FS shape | Bragg velocity | Bragg width | Bragg shape KpK fit | FS-to-Bragg ratio | CNR |
|---|---|---|---|---|---|---|---|---|
| Upwind | 162 Hz (2.7 m/s) | ±35 Hz (±0.6 m/s) | 1.3 | 58 Hz (1.0 m/s) | ±59 Hz (±1 m/s) | 9 | −6 dB | 13.5 dB |
| Downwind | −123 Hz (−2.0 m/s) | ±22 Hz (±0.4 m/s) | 4 | −17 Hz (−0.3 m/s) | ±50 Hz (±0.8 m/s) | 11.5 | −4.8 dB | 11.5 dB |

## V. COHERENT PROCESSING AND SUBOPTIMAL DETECTOR STRUCTURES

A significant body of published work has examined the development of coherent detectors for application to surveillance of maritime surface targets [7, 24–26]. Most of this past development has focussed on the analysis of single-channel data collected from stationary or slow-moving platforms, with processing applied in the full measurement space, i.e., corresponding to measurement vectors of temporally contiguous pulses comprising a full CPI. In contrast, the motivation for this study is the development of signal processing algorithms for maritime surveillance from high-altitude, rapidly moving platforms and the investigation of the potential of multichannel radars for this application. As discussed in Section IV, rapid platform motion coupled with antenna azimuth beamwidth can result in significant Doppler broadening of the clutter spectrum. From comparison of the observed and inherent spectra of Fig. 3, we observe that total bandwidth from the moving platform is significantly larger than the bandwidth that would be observed for a stationary platform. This leakage of the clutter signature into higher-velocity Doppler bins could cause significant detection performance degradation over a range of velocities of practical interest.

Because multiaperture STAP allows clutter and target signals to be both temporally and spatially separated, it may be helpful in mitigating the aforementioned Doppler broadening effects. This contrasts with single-aperture systems, which are unable to distinguish between spectral broadening because of internal clutter motions (ICMs) on the sea surface and that because of Doppler broadening. For typical GMTI applications, the inherent spectrum of the ground clutter is narrow, and moving ground target velocities are typically larger than those of maritime targets. This combination of factors generally results in excellent separation of land target and ground clutter through the spatial–temporal adaptation. In contrast, it is evident from Fig. 3 that for maritime applications, complete separation of the target signal from the underlying clutter via spatial–temporal steering vectors is only possible in frequency regions that lie outside the inherent bandwidth of the sea clutter. Because maritime surveillance concept of operations is frequently concerned with the monitoring of stationary or low-velocity surface targets, coherent processing often provides more limited gains in comparison with GMTI. We return to this point in the discussion of results in Section VI.D.

As mentioned earlier, most past work has focussed on single-channel coherent maritime surveillance processing, with adaptation of the full-rank covariance matrix estimated using full-length CPIs. The most common method for obtaining an estimate of the covariance matrix is to use secondary data from the target-free range cells on either side of the CUT. If the theoretical conditions of range-homogenous, CN clutter statistics can be met, the calculation of an accurate estimated full-rank covariance matrix is trivial, because one can use as many background cells as required to meet the desired performance. For instance, Reed et al. [27] showed that a sample support size of twice the CPI length is required to achieve performance equivalent to a perfectly known, i.e., clairvoyant, covariance matrix with an inherent signal-to-interference-plus-noise ratio (SINR) 3 dB less than the data under test. This background size requirement can be reduced somewhat through approaches such as diagonal loading and autoregressive (AR) estimation of the covariance matrix (e.g., see [28–30]) but performance still exhibits a dependency on the number of representative background samples available. The use of diagonal loading with reduced background sample sizes was investigated in this study but was found to decrease performance against the current data. Loading is not further considered in this work.

The fully adaptive approach and associated background support size requirements are problematic from a practical standpoint in two regards:

1) The covariance matrix dimensions are large, leading to a computationally expensive matrix inversion step.
2) The background sample support size requirement becomes quite large.

The background sample support size issue is not trivial, because maximum likelihood (ML) estimation of the sample covariance matrix (SCM) via equal weight averaging of background sample covariance matrices implicitly assumes that clutter statistics remain stationary across the background support. This condition is frequently violated in real-world conditions. The issue is exacerbated for STAP systems, because data are collected on multiple receive channels, thereby increasing the covariance matrix dimensionality and associated sample support size requirements.

## A. Suboptimal Space–Time Adaptive Processors

The practical limitations of fully adaptive STAP have long been recognised in the GMTI community, and suboptimal approaches have been developed and employed to reduce the dimensionality of the adaptation problem. The use of these suboptimal approaches does not seem to have been generally addressed in the corresponding maritime literature, which primarily focuses on fully adaptive approaches. An exception is the work of Conte et al. [31], who examines the advantages of using Fourier decompositions for single-channel detector design. Practically speaking, suboptimal STAP frequently gives superior real-world performance for GMTI in comparison with the theoretically superior fully adaptive approaches. Not withstanding the well-documented application of these approaches to GMTI problem, it is unclear how effectively they perform against sea clutter. A quantitative assessment of their potential is undertaken in this paper.

In the following section, we examine the detection performance obtained using three suboptimal STAP architectures:

1) Adjacent bin post-Doppler (ABPD) STAP
2) PRI-staggered post-Doppler (PSPD) STAP
3) Pre-Doppler (PreD) STAP

A detailed description of the preceding techniques is beyond the scope of this paper; refer to Ward [19] for an excellent review of the topic. In particular, Figs. 34, 45, and 46 of the Ward report present flowcharts for PreD, PSPD, and ABPD processing, respectively. Generally, the post-Doppler approaches employ a FFT to convert the initial measurement to the frequency domain before the application of adaptation, or whitening, and the generation of the applicable detection statistic. For PSPD, the individual frequency bins are assumed to be independent of one another, thereby allowing the spatial adaptation to be separately applied to each frequency bin. A degree of temporal adaptivity is introduced by taking the FFT of several overlapping sub-CPIs, typically called taps. Measurement vectors for each frequency bin are then formed by combining all taps and channels for given frequency. ABPD is similar to PSPD in that adaptation is performed after transformation of the data vector to the frequency domain. However, in the case of ABPD, an additional dimension of adaptivity across frequency is achieved by combining a small number of contiguous frequency bins to form the final measurement vector for whitening.

PreD differs from the post-Doppler approaches in that the whitening process is carried out in the time domain. To reduce the dimensionality of the problem, each full CPI is divided into smaller overlapping sub-CPIs for which individual ML estimates of the complex target amplitude are obtained; i.e., the whitening matched filter is applied to each sub-CPI. The outputs from all sub-CPIs are then coherently combined per a postulated target frequency to retrieve the full coherent gain corresponding to the original CPI length.

For all preceding suboptimal techniques, the size of the SCM to be estimated and inverted is significantly reduced with respect to the fully adaptive problem, thereby addressing items 1 and 2 of Section V.

## B. Pulse-Doppler Processing

In analogy with the post-Doppler STAP techniques, we evaluate the corresponding pulse-Doppler performance that would be obtained from a single-channel system. This approach corresponds to taking the FFT of the CPI of single-channel data to convert data to the Doppler frequency domain. The test statistic corresponding to each CUT is formed by dividing each CUT in a Doppler bin by a normalising factor formed using a CA approach. Because the data used for this study was collected using a linear three-channel array, we synthesise a corresponding single-aperture antenna by coherently adding the returns from all three receive channels. The apertures of the three phase centres of the PAMIR antenna are closely spaced, resulting in essentially no grating sidelobes.

## C. Suboptimal Detector Structures

All three STAP techniques are primarily concerned with the formation of the optimal whitening matched filter to transform the raw measurement vector to a whitened or clutter suppressed subspace. Once accomplished, it is necessary to make a detection decision based on the transformed measurement vector. For this paper, we employ the well-known adaptive matched filter (AMF).

The AMF detector derives from the generalised likelihood ratio test (GLRT) formed assuming a CN formulation for the clutter statistics [32] and takes the form

$$T_{\text{AMF}}(\mathbf{z}) = \frac{\left|\mathbf{b}^\dagger \mathbf{R}^{-1} \mathbf{z}\right|^2}{\mathbf{b}^\dagger \mathbf{R}^{-1} \mathbf{b}} \underset{H_0}{\overset{H_1}{\lessgtr}} \eta, \qquad (2)$$

where $\mathbf{b}$ is the steering vector, $\mathbf{R}$ is the clutter-plus-noise covariance matrix, $\mathbf{z}$ is the complex measurement vector, and $\eta$ is the threshold to achieve specified PFA.

The AMF structure arises when a ML estimate of the unknown signal amplitude is used, i.e., the GLRT, and the covariance matrix is assumed to be perfectly known. For a practical implementation, the covariance matrix is generally unknown and the SCM is estimated from $K$ background samples per

$$\widehat{R} = \frac{1}{K} \sum \mathbf{z}\mathbf{z}^\dagger. \qquad (3)$$

The SCM represents the ML estimate of the covariance matrix under the condition of range-homogenous CN clutter. As shown in Section IV.B, sea clutter backscatter is often poorly represented by CN statistics, and one would anticipate that detector performance could therefore degrade from the ideal. This is seen to be the case in Section VI, where the performance of the AMF against the
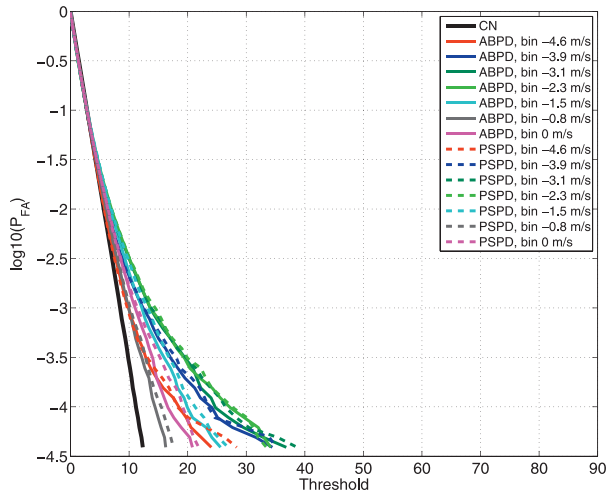
Fig. 9. Comparison of PFA versus threshold for ABPD and PSPD test statistics across negative endoclutter velocities. Downwind viewing geometry.
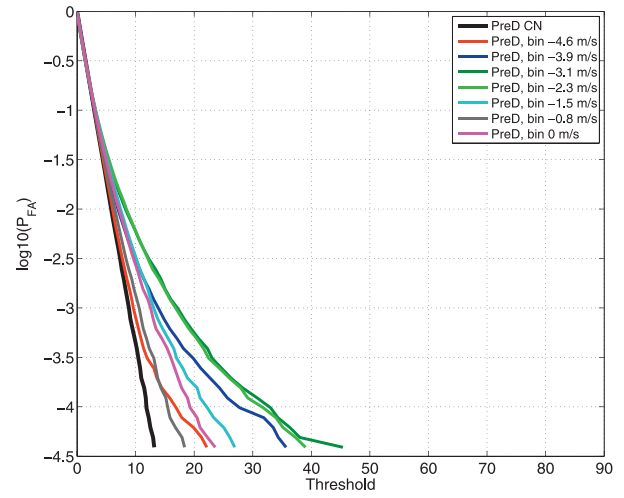


Fig. 10. Comparison of PFA versus threshold for PreD test statistics across negative endoclutter velocities. Downwind viewing geometry.

PAMIR data is seen to depart significantly from the desired CFAR response.

## VI. PERFORMANCE COMPARISON FOR SUBOPTIMAL AMF PROCESSING

### A. CFAR Characteristics

In this section, we examine the PFA versus threshold dependency of the test statistic obtained using each of the STAP approaches. The application of the PreD approach was found to require a final CA normalisation step. To the authors' knowledge, the need for this further normalisation step does not seem to be discussed in the open literature, although presumably some scheme is implemented in operational systems. The requirement for this normalisation is discussed in Appendix A.

Figs. 9–12 present the post-Doppler and PreD CCDF curves for the downwind and upwind data sets. Fig. 9 presents the downwind results for ABPD and PSPD processing for the velocity range −4.6 to −0.8 m/s. This velocity range significantly overlaps with the observed clutter spectrum, i.e., endoclutter. Fig. 10 presents the corresponding results for the downwind PreD results. Throughout the endoclutter region, the PFA versus threshold curves for all three approaches depart, sometimes significantly, from the theoretical CN curve. The CCDF curves are observed to approach the CN curve more closely as the velocities approach the exoclutter region. This behaviour is anticipated, and even better agreement with the theoretical was observed for fully exoclutter velocities, although these results are not presented for conciseness. Similar behaviour is observed for the upwind complimentary (positive) endoclutter velocities in Figs. 11 and 12, although the CCDF curves are observed to be more spiky, i.e., have longer tails. This is further addressed in the later discussion.

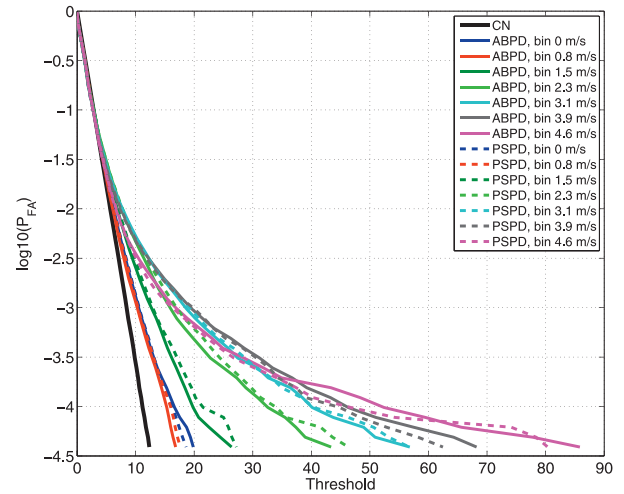The preceding behaviour is summarised in Figs. 13 and 14, where the measured PFAs obtained for theoretical



Fig. 11. Comparison of PFA versus threshold for ABPD and PSPD test statistics across positive endoclutter velocities. Upwind viewing geometry.
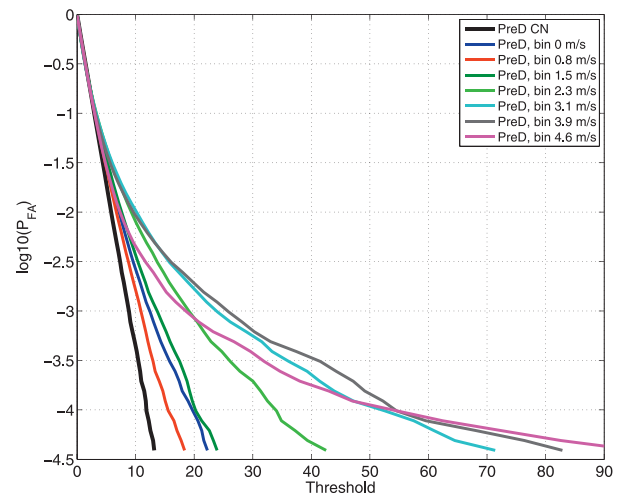


Fig. 12. Comparison of PFA versus threshold for PreD test statistics across positive endoclutter velocities. Upwind viewing geometry.
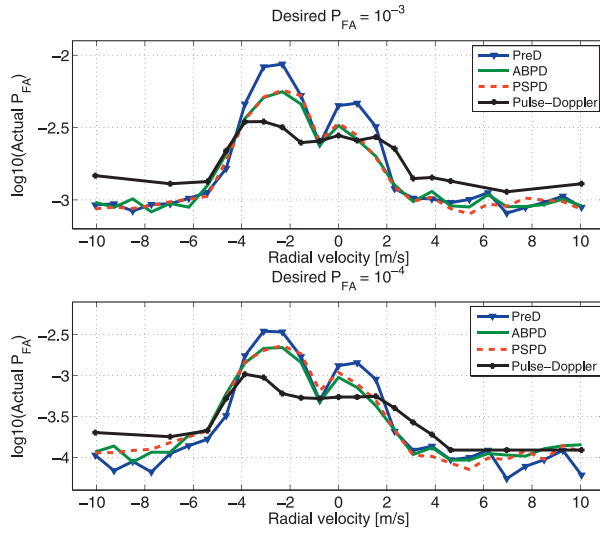
Fig. 13. Actual PFA achieved versus Doppler velocity for PreD, ABPD, PSPD, and pulse-Doppler, with threshold set to achieve PFA = $10^{-3}$ and PFA = $10^{-4}$ for CN clutter statistics. Downwind viewing geometry.
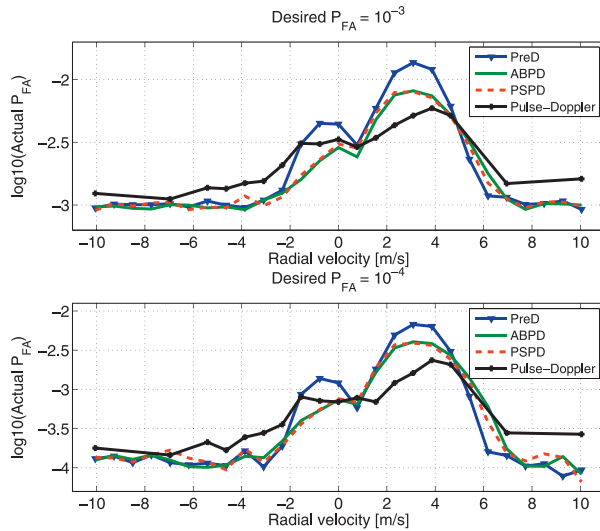


Fig. 14. Actual PFA achieved versus Doppler velocity for PreD, ABPD, PSPD, and pulse-Doppler, with threshold set to achieve PFA = $10^{-3}$ and PFA = $10^{-4}$ for CN clutter statistics. Upwind viewing geometry.

thresholds corresponding to PFAs of $10^{-3}$ and $10^{-4}$ are plotted across the $\pm 10$ m/s velocity band for both STAP and pulse-Doppler approaches. Some key features of interest are as follows:

1) Peak PFA mismatch: The Doppler velocity of the peak PFA mismatch under STAP is different from that observed under pulse-Doppler processing.

2) CFAR characteristics: PreD approach shows greater variation from desired PFA in comparison with post-Doppler and pulse-Doppler approaches. The relative endoclutter performance of pulse-Doppler versus STAP approaches depends on the velocity bands in question. Downwind pulse-Doppler CFAR performance is observed to be superior to STAP for more negative endoclutter

velocities but inferior for more positive endoclutter velocities. Conversely, upwind pulse-Doppler CFAR performance is observed to be superior to STAP for more positive endoclutter velocities but inferior for more negative endoclutter velocities.

3) Viewing geometry dependence: Both PreD and post-Doppler statistics exhibit greater spikiness for the upwind direction.

The implications of the preceding observations are discussed in the next section.

### B. Discussion of CFAR Characteristics

The CFAR performance trends for all approaches presented in Figs. 13 and 14 are observed to be broadly consistent with intuitive expectations, with regions of excessive PFA exhibiting good alignment with the regions of low effective shape parameter per Figs. 6 and 7, i.e., $-5$ to 2 m/s for the downwind geometry and $-2$ to 5 m/s for the upwind geometry. Both PreD and post-Doppler endoclutter CCDF curves in Figs. 11 and 12 exhibit enhanced spikiness in the upwind direction, as do the pulse-Doppler results, and are consistent with the increased prevalence of burst scattering for upwind viewing geometries, as discussed in Section III. Moving beyond this general comparison, there are significant differences in the detailed behaviour of the CFAR performance for the different processing approaches.

It is of particular interest to compare the velocity locations at which the peak PFA mismatches occur for PreD, post-Doppler, and pulse-Doppler processing. For pulse-Doppler processing, the peak PFA mismatch is observed to align closely with the location of the minimum effective shape of Figs. 6 and 7. In contrast, both the PreD and the post-Doppler PFA peaks are found to closely align with the centre frequency of the fitted FS component of the two-component model in Table IV, corresponding to $-2.0$ m/s and approximately 2.7 m/s for the downwind and upwind directions, respectively. The primary difference between STAP and pulse-Doppler processing is that the spatial steering vector is applied before whitening for pulse-Doppler and after whitening for STAP. In other words, the changes in PFA behaviour that are observed for STAP are introduced as a result of the whitening process. This observation is not readily anticipated as a result of the proposed two-component clutter model and suggests that the Bragg component has been preferentially cancelled in comparison to the FS component during STAP. The effect is particularly pronounced for post-Doppler processing, with the velocity location of the PreD PFA mismatch peaks intermediate to the post-Doppler and pulse-Doppler results. The factors responsible for the observed offset between the PreD and the post-Doppler peaks are difficult to quantitatively identify and a topic for future investigation.

Further evidence of the preferential cancellation of the Bragg component can be deduced from the relative CFAR performance of the STAP and pulse-Doppler approaches

across the full endoclutter velocity band, which is defined to lie between approximately −6 and 6 m/s. Referring to Fig. 13 for the downwind geometry over the subregion of the endoclutter band corresponding to −4 to 1 m/s, pulse-Doppler displays superior CFAR performance with respect to post-Doppler processing, while for the complementary velocity regime, the behaviour is reversed. Referring again to Fig. 6, we observe that superior pulse-Doppler performance is associated with regions where the FS contribution is strongest and, conversely, the superior post-Doppler performance occurs in the region where the Bragg contribution is dominant. Furthermore, the behaviour is not correlated to total clutter power, because velocities with equivalent combined clutter power are observed to lie in different regimes. Similar behaviour is observed for the upwind direction and PreD results. The impact of differing assumptions with respect to the characteristics of underlying clutter components is examined in more detail in the companion paper of this series.

None of the approaches achieve stable CFAR performance under AMF detection. If the clutter statistics conform to a SIRP, then the ANMF detection approach would provide more appropriate test statistics. The SIRP assumption and the application of the ANMF test statistic is examined in detail in the companion paper [18]. Overall, the PreD approach is observed to exhibit inferior CFAR behaviour in comparison with post-Doppler approaches. The inferior PreD performance may be the result of the final normalisation step described in Section VI.A. A possible ad hoc approach for control of PFA settings would be to empirically characterise the PFA versus threshold relationship for each Doppler bin in real time and set the threshold accordingly. These types of approaches have been used extensively for real-world noncoherent radars and require the availability of a sufficient number of statistically independent target-free samples representative of the CUT. Alternately, the parameters of an appropriate stochastic model can be empirically determined and the applicable threshold can be calculated. This approach typically requires smaller sample support but depends on the ability to identify a pdf that accurately predicts the behaviour for very small PFAs [1].

All results in this paper correspond to a 0° steering vector after compensation of the antenna look direction. In contrast, an operational STAP system typically surveys a range of steering angles. As discussed in Section IV.B, the relative contribution of FS versus slow scattering components is a function of both Doppler frequency and steered direction of the beam pattern. The implication is that any ad hoc characterisation of the PFA versus threshold relationship will likely need to be undertaken individually for all measured steering angles and Doppler velocities under STAP. These approaches present significant practical challenges in the design of robust operational processors. The practical considerations surrounding the calculation of the required detection
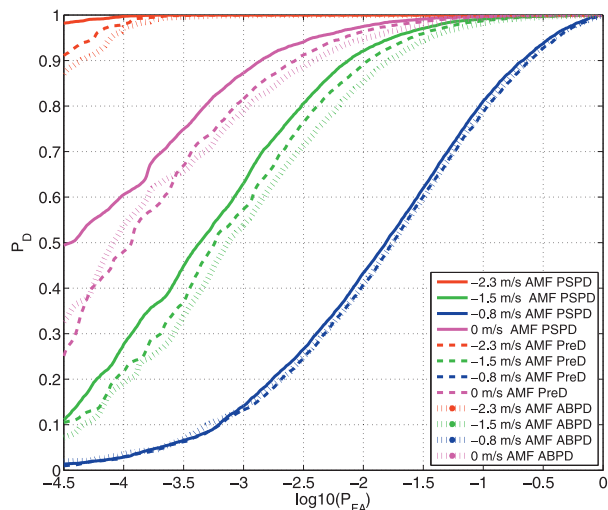


Fig. 15. ROC curves for PreD, ABPD, and PSPD with downwind viewing geometry. SNR is 25 dB per Doppler bin.

threshold for CFAR operation are not further examined in this paper and remain a topic for future study.

In summary, some key observations to draw from the preceding discussion are as follows:

1) PreD STAP produced the worst CFAR performance.
2) Post-Doppler produced best CFAR performance in a Bragg-dominated region.
3) Pulse-Doppler produced best performance in a FS-dominated region.
4) STAP-based approaches appear to preferentially whiten Bragg-generated backscatter.

### C. Detection Performance

To assess the detection performance of the competing approaches, it was necessary to inject ideal moving targets into the PAMIR data at velocities corresponding to the centre frequencies of the corresponding Doppler bins after application of the full CPI FFT. The resulting ROC curves are presented in Figs. 15–18 for the PreD, ABPD, and PSPD approaches. Noncoherent processing techniques were found to produce effectively no detection capability for the signal-to-noise ratios (SNRs) investigated in this paper and are not further discussed. Results are presented for a selected range of target velocities and SNRs, which highlight the key points of the ensuing discussion. The lower axis corresponds to the empirically observed PFA, not the effective PFA achieved using a theoretical threshold. Because of the variations of CNR with Doppler frequency, it is necessary to use larger SNRs for endoclutter velocities to achieve significant results. Processing parameters are given in Table V. Figs. 19 and 20 summarise the detection performance differences between the suboptimal STAP approaches at fixed PFA of $10^{-4.5}$ for the upwind and downwind directions, respectively. The numerous flat sections with zero value typically correspond to regions in which the probability of
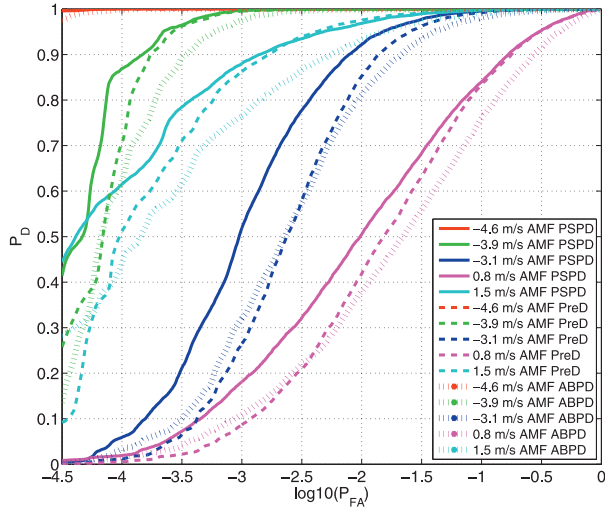
Fig. 16. ROC curves for PreD, ABPD, and PSPD with downwind viewing geometry. SNR is 13 dB per Doppler bin.
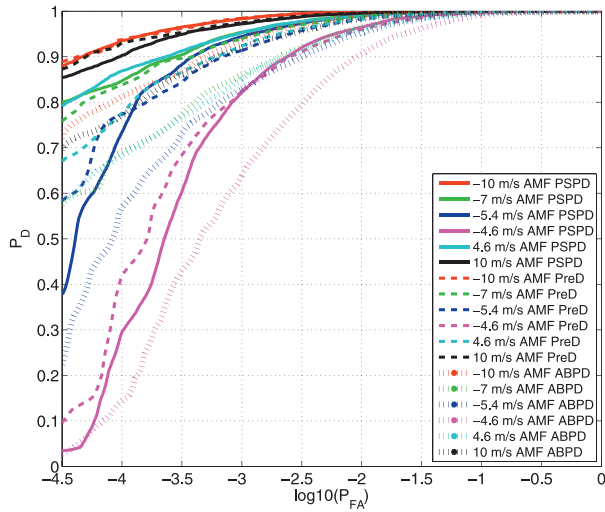


Fig. 17. ROC curves for PreD, ABPD, and PSPD with downwind viewing geometry. SNR is 7 dB per Doppler bin.
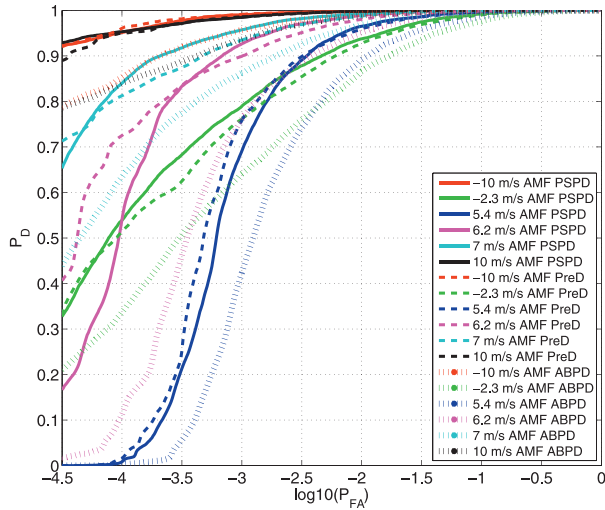


Fig. 18. ROC curves for PreD, ABPD, and PSPD with upwind viewing geometry. SNR is 7 dB per Doppler bin.

TABLE V
STAP Parameters

| Full CPI length | 64 pulses |
|---|---|
| Number of channels | 3 |
| Number of contiguous frequencies for ABPD | 3 |
| Dimensionality of ABPD adaptation | 9 |
| Number of taps for PSPD | 3 |
| PSPD sub-CPI lengths | 62 pulses |
| Dimensionality of PSPD adaptation | 9 |
| Number of sub-CPIs for PreD | 57 |
| PreD sub-CPI length | 8 pulses |
| Dimensionality of PreD adaptation | 24 |
| Number of background range samples | 128 |
| Guard cells | 2 each side of CUT |
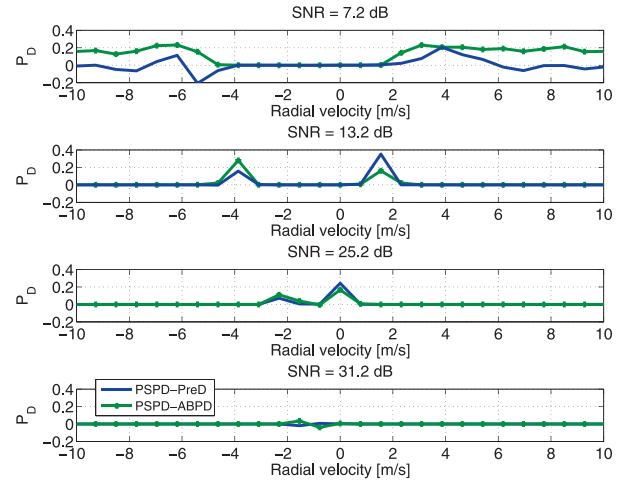


Fig. 19. PD versus Doppler velocity for PreD and ABPD with respect to PSPD for downwind viewing geometry. Measured PFA is $10^{-4.5}$.
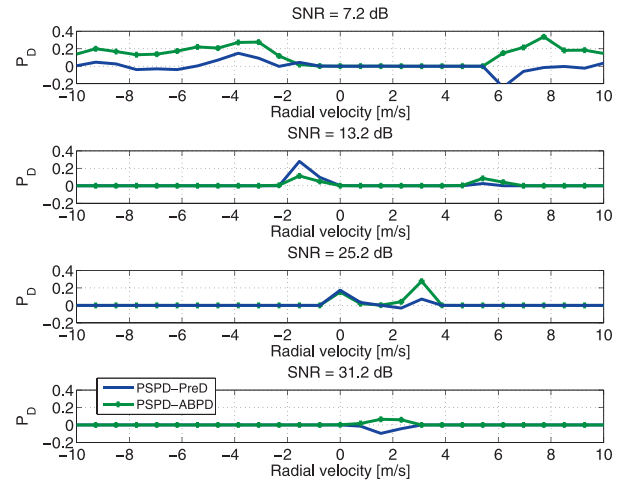


Fig. 20. PD versus Doppler velocity for PreD and ABPD with respect to PSPD with upwind viewing geometry. Measured PFA is $10^{-4.5}$.

detection (PD) of all approaches have saturated at a value of 1 or 0 rendering these results nugatory. This also leads to an apparent phenomenon in which the PD peaks for the higher SNR appear to approach each other.

In general, PSPD provides superior detection performance over the broadest range of velocities and
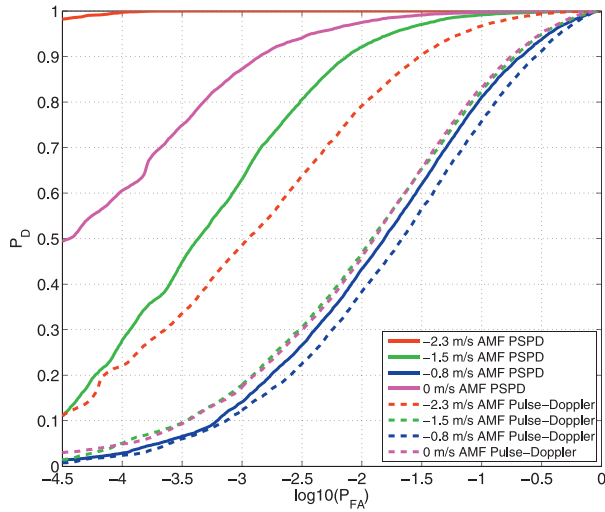
Fig. 21. ROC curves for pulse-Doppler and PSPD with downwind viewing geometry. SNR is 25 dB per Doppler bin.



Fig. 22. ROC curves for pulse-Doppler and PSPD with downwind viewing geometry. SNR is 7 dB per Doppler bin.

ABPD gives the poorest performance. For most velocities, PreD detection performance is inferior or similar to PSPD performance, with the exception of two narrow velocity bands corresponding to −5.4 to −4.6 m/s in the downwind direction and 6.2 to 7.0 m/s in the upwind direction, where PreD exhibits superior detection performance. These regions are readily identifiable as negative values of the blue curves. This behaviour is discussed in more detail in Section VI.D. Referring back to the ROCs of Figs. 15–17, it can be seen that reversals of PSPD and PreD relative performance are occasionally seen for larger PD, with PreD providing a small relative improvement in detection performance in these regions. A similar crossover is occasionally observed at lower PD for PreD and ABPD, with PreD exhibiting an increasing PD gain as the absolute PD value increases. The reasons for these crossovers have not been ascertained. In general, the PD differences tend to be small in the affected regions and correspond to unacceptably large PFAs for operational use.

The relative performance of STAP versus pulse-Doppler is compared in Figs. 21 and 22 for the downwind direction. ROC curves are not presented for the upwind direction, because similar behaviour to downwind results is observed. For clarity, only PSPD and pulse-Doppler are compared, because PSPD was shown to exhibit the best overall performance amongst the suboptimal STAP processors. For all velocity bands and PFA, PSPD exhibits superior or equivalent performance to pulse-Doppler. Figs. 23 and 24 summarise the PD performance across a range of velocities for a PFA of $10^{-4.5}$ for both downwind and upwind directions. The performance has a bimodal character, with a local minimum near, but not exactly aligned with, the peak of the clutter spectrum. Little performance gain is realised through the use of STAP approaches for very slow or stationary targets, as anticipated. As one moves towards more negative or positive Doppler velocities, significant
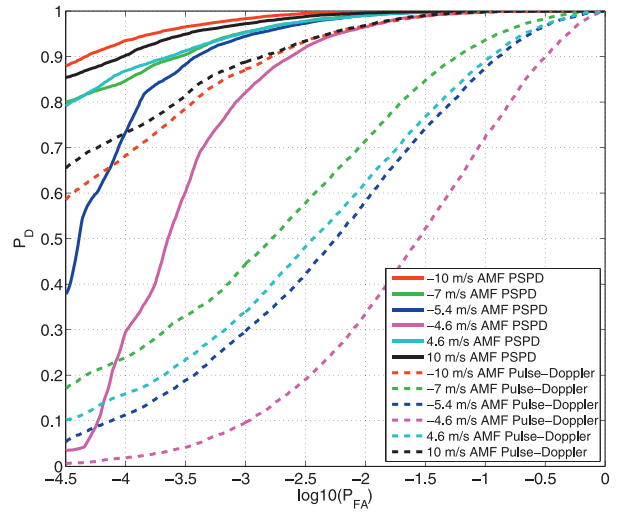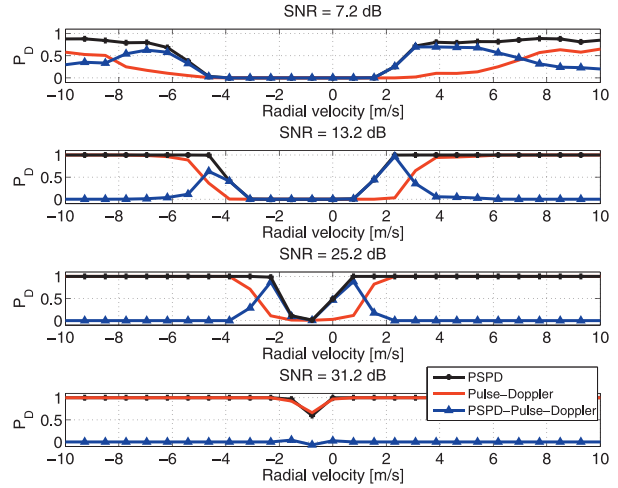


Fig. 23. PD versus Doppler velocity for pulse-Doppler (red curve) and PSPD (black curve) with downwind viewing geometry. Blue curve gives difference between PSPD and pulse-Doppler. Measured PFA is $10^{-4.5}$.
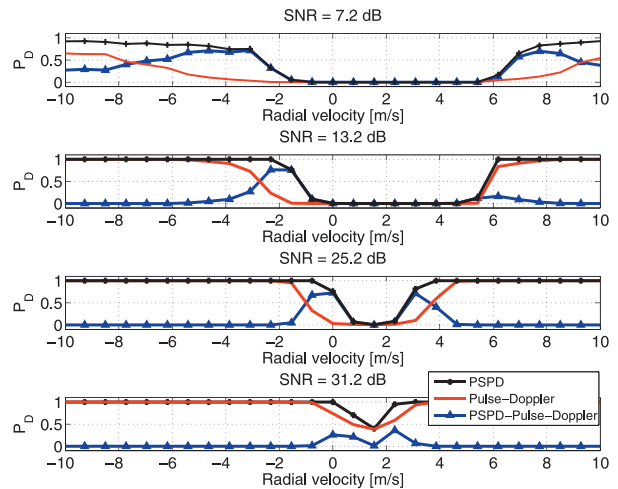


Fig. 24. PD versus Doppler velocity for pulse-Doppler (red curve) and PSPD (black curve) with upwind viewing geometry. Blue curve gives difference between PSPD and pulse-Doppler. Measured PFA is $10^{-4.5}$.
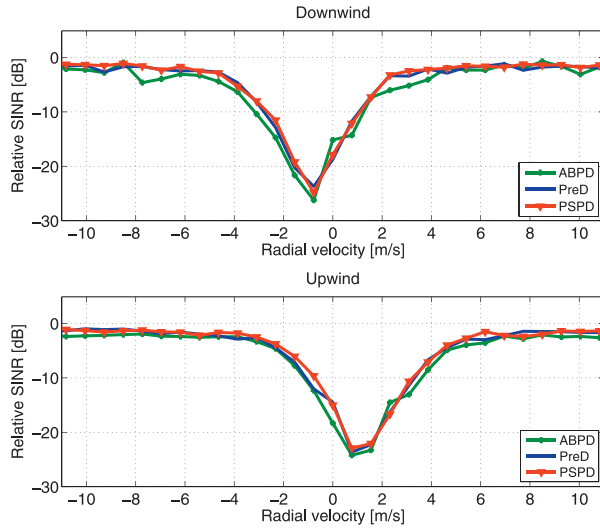
Fig. 25. Relative SINR versus target velocity for broadside viewing configuration, with target at beam centre derived using PAMIR data. All relative values are with respect to performance in clutter-free data, i.e., only receiver noise. Top: Downwind viewing geometry. Bottom: Upwind viewing geometry.

performance gains are initially observed for PSPD with respect to pulse-Doppler, followed by a gradual decrease as one approaches exoclutter velocities. This behaviour is discussed in further detail in the next section.

### D. Discussion of Detection Performance

To facilitate our understanding of the factors affecting observed detection performance, it is useful to examine the SINR curves for each of the suboptimal STAP architectures of Section V.A. The SINR curves were calculated using the actual PAMIR data. The SINR for each approach is defined per (112) and (185) of Ward's report [19]. Fig. 25 presents the curves for downwind and upwind directions.

McDonald and Cerutti-Maori [5] previously presented the theoretical SINR curve that would be obtained for land clutter collected using an identical broadside viewing geometry with an equivalent CNR to the PAMIR data examined in this paper. Because the land clutter was assumed to be the result of stationary clutter objects, the resulting curve exhibited a clutter notch symmetrical about and centred at 0 Hz. In comparison, the clutter notch in Fig. 25 is shifted to negative and positive velocities for the downwind and upwind geometries, respectively, consistent with the observations of Section IV. The PAMIR SINR responses are also observed to be asymmetrical with respect to the notch minimum and broader than the land clutter SINR results. The broadening is anticipated because of the inherent spectral width of the sea clutter spectrum, and the slight asymmetry is anticipated by the discussion of Section IV with regards to FS and Bragg scattering mechanisms.

With regards to relative performance of the suboptimal approaches, ABPD is seen to generally produce the worst

SINR performance, consistent with the detection results presented in Section VI.C. Two apparent exceptions, at 0 m/s for the downwind geometry and 2.3 m/s for the upwind geometry, are inconsistent with the trend of the overall curves and appear to be lingering artefacts of outliers. In contrast, PSPD and PreD processing produce similar SINR performance.

The preceding results highlight the limitations of using SINR measures as the sole guides to processing performance. While the SINR analysis is successful in predicting the inferior detection performance of ABPD, it fails to convincingly discriminate between PSPD and PreD performance. PreD is expected to exhibit a small SINR loss in comparison with PSPD under conditions of highly coherent target signal and CN clutter due to the significant spreading of the target signal across clutter bins that arises because of the short sub-CPI lengths. This SINR loss is not readily observable in Fig. 25.

While the broad SINR trends of Fig. 25 are generally consistent with the performance characteristics of Section VI.C, with an increase in detection performance observed as target Doppler moves away from the clutter spectrum peak, a more detailed quantitative assessment shows that the SINR curves fail to predict the observed asymmetries of detection performance with respect to the clutter notch. As an example, consider the PSPD SINR curve of Fig. 25. The SINR values at the $-3$ and $+1.5$ m/s points have approximately equal SINR. Based purely on this metric, one would expect roughly identical detection performance for the two velocities. Different detection performance is observed in Fig. 16, with the $-3$ m/s ROC curve having a consistently lower PD than the $+1.55$ m/s curve for all reasonable PFA levels; e.g., PD is 0.06 and 0.6 for the $-3$ and $+1.55$ m/s, respectively, at a PFA of $10^{-4}$. A similar effect is observed for PreD and ABPD processing. This behaviour is easily understood by referring back to the CCDF curves of Section VI.A. In particular, we see from Figs. 9 and 11 that the required threshold to achieve a PFA of $10^{-4}$ is 26.5 and 15.6 for the $-3$ and $+1.5$ m/s velocities, respectively. This observation is consistent with detection performance, under most common conditions, degrading as the statistics become spikier.

As noted earlier, PSPD processing gives the best detection performance over the broadest range of Doppler frequencies. Two notable exceptions were identified at $-5.4$ and $+6.2$ m/s for the downwind and upwind results, respectively, where PreD exhibits an absolute detection performance enhancement of greater than 0.2. This result is not predicted by the SINR responses. The corresponding ROC curves can be observed in Figs. 17 and 18. Some clues to interpreting this behaviour can be derived from Figs. 13 and 14, in which it is observed that the velocities correspond to localised regions where the PreD PFA mismatches are seen to be less than the post-Doppler approaches; i.e., the PreD CCDF curve at this velocity is less spiky than the post-Doppler responses. The reason for this behaviour remains unresolved.

Returning to Figs. 23 and 24, PSPD performance gains for velocities centred at the range $\pm 1.5$ m/s were quite limited with respect to pulse-Doppler. This result is best understood by reference to the lower left panel of Fig. 3, where the estimated inherent clutter spectrum is presented. The $\pm 1.5$ m/s band can be seen to be internal to the inherent spectrum, and as such, the target signal cannot be effectively separated from the clutter response through temporal or spatial–temporal steering. Beyond this velocity band, it becomes possible to spatially separate the clutter and target signal, resulting in significant performance gains. This latter effect is well known and is the primary motivation for the use of STAP for GMTI. The primary difference under maritime conditions is that the inherent spectrum is wider and more likely to overlap with target velocities of interest. As one moves beyond the $\pm 10$ m/s velocities (not shown) into a true exoclutter region, the detection performance of the pulse-Doppler techniques and that of the STAP techniques are seen to converge as expected.

In summary, some key observations to draw from the preceding discussion are as follows:

1) PSPD provides the best detection performance of the STAP techniques, and ABPD provides the worst.

2) Differences of detection performance between STAP techniques tend to be small when detection threshold settings are accurately known.

3) PSPD detection gains with respect to pulse-Doppler are negligible when target velocity lies within bandwidth of the inherent clutter spectrum.

4) Detection performance degradation in operational systems is likely to be dominated by poor CFAR control, leading to incorrect detection threshold settings.

## VII.  CONCLUSIONS

A comprehensive analysis was undertaken of backscatter characteristics of real maritime sea clutter data collected using FHR PAMIR operating from a fixed wing platform. The variation of backscatter power and statistics with Doppler frequency for the PAMIR data set were shown to be inconsistent with CN formulations and were found to be best modelled using a KpK two-component model. The inclusion of effective shape parameter variation with frequency as a fitting constraint was seen to significantly limit the range of acceptable model fits, effectively eliminating one-component clutter models as viable proposals. The characteristics of the fitted components, e.g., spectrum centre and spectrum width, were used to explain several features of observed detector outputs for the PAMIR data set.

The PAMIR data were also used to evaluate the performance of several suboptimal coherent detector structures. Three STAP techniques were examined, corresponding to PSPD, ABPD, and PreD. All approaches were shown to exhibit non-CFAR performance versus changes in Doppler velocity. The non-CFAR performance is shown to be consistent with the presence of FS and
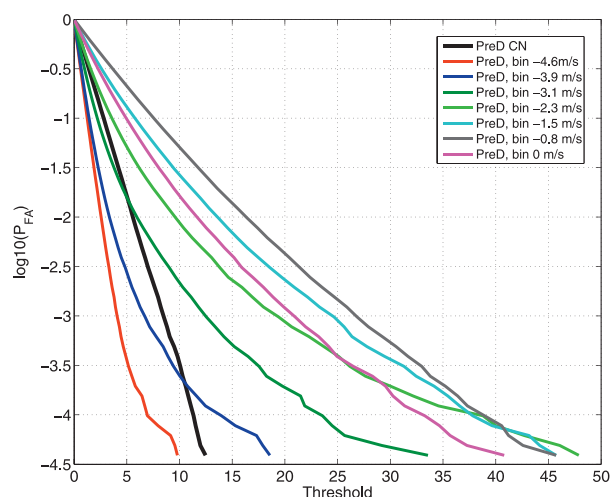


Fig. 26.  Comparison of PFA versus threshold for ideal CN clutter statistics and measured PreD unnormalised test statistics across negative endoclutter velocities. Downwind viewing geometry.

Bragg scattering mechanisms in the sea clutter and the action of Doppler broadening due to aircraft motion. The PRI-staggered approach provided the best overall performance in terms of both detection and nearest approach to CFAR performance. PSPD processing was shown to provide significant detection performance improvements in comparison with pulse-Doppler for Doppler velocities greater than the inherent bandwidth of the sea clutter spectrum, with relative gains rapidly diminishing for velocities internal to the inherent spectrum. In contrast, the pulse-Doppler approach was shown to exhibit less false alarm rate variation over a significant portion of the endoclutter Doppler spectrum.

Overall, PSPD STAP is demonstrated to be the superior STAP approach of the techniques examined for the data set in question. Although PSPD STAP is shown to provide superior detection performance with respect to pulse-Doppler, the final decision on detection architecture must balance the potential detection gains against the superior CFAR performance of the pulse-Doppler system, as well as the reduced complexity of single-channel systems.

## APPENDIX A.  CA NORMALISATION FOR PRED PROCESSING

Per the open literature, and consistent with the discussion of Section V.A, the final step in PreD processing is commonly presented as the application of a temporal steering vector of appropriate Doppler frequency across the measurement vector composed of all sub-CPIs test statistics for the corresponding Doppler bin in question. Fig. 26 presents an example of the CCDF curves obtained per this methodology for the downwind geometry, along with the theoretical curve for CN clutter. It is readily apparent that observed behaviour is not the CFAR with respect to velocity, because the CCDF curves corresponding to different Doppler velocities appear to be
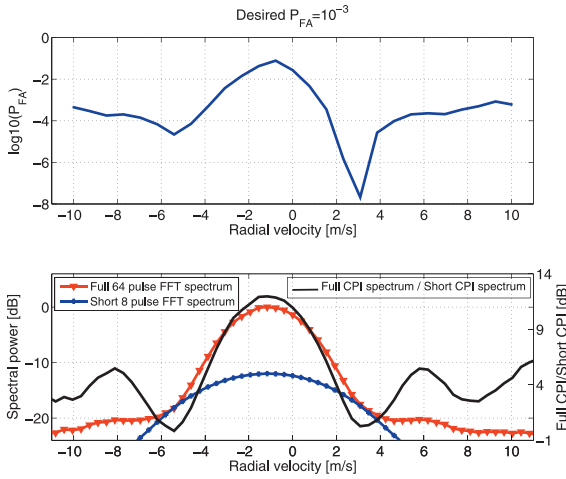
Fig. 27.  Top: Actual PFA versus velocity for unnormalised PreD for downwind viewing geometry, with threshold set to achieve theoretical PFA = $10^{-3}$. Bottom: Spectral response for 8- and 64-pulse window on measurement for downwind viewing geometry.

scaled to smaller and larger thresholds with respect to the CN curve. This behaviour is summarised in the top panel of Fig. 27 for the velocity range of $\pm 10$ m/s and a theoretical threshold setting corresponding to a PFA of $10^{-3}$. The actual PFA is seen to widely fluctuate above and below the desired level.

The root of this behaviour can be explained by referring to the bottom panel of Fig. 27, where spectra are presented for a simulated single-channel system with Doppler broadening and SNR similar to that of the PAMIR data. Two spectra are presented corresponding to the FFT output observed for an 8-pulse sub-CPI versus a full 64-pulse CPI. These responses correspond to the spectra for the 8-pulse PreD sub-CPI and the post-Doppler, respectively. The black curve of the bottom panel corresponds to the ratio of the full CPI and short CPI spectra. This latter result provides a measure of the mismatch between the sub-CPI whitening and that required for full-resolution output. The observed PFA mismatches of the top panel are largely explained by this effect, with remaining discrepancies attributable to PreD corresponding to a spatial–temporal whitening (as opposed to the temporal whitening presented here) and the presence of FS. This latter effect is especially evident in the asymmetrical response of the CCDF curve of the top panel at $-5.4$ and 3.1 m/s. Per Fig. 6, the ratio of FS to Bragg power is higher for $-5.4$ m/s. The muted response at this Doppler velocity is indicative of a spikier test statistic. This effect is discussed in further detail in Section VI.B.

The poor CFAR versus Doppler frequency response described earlier is highly undesirable, and some form of normalisation is required to remove the observed scaling error. In theory, the optimal approach would be to estimate and apply a whitening matched filter during the final coherent integration. Practically, this approach is problematic because of long vector length and associated background sample support, as discussed in Section V.A.

The avoidance of this condition was the motivation for using PreD. A simpler approach, which was used for the analysis in this paper, is to normalise the test statistics for each Doppler bin using an estimate of the mean underlying clutter power obtained per a CA approach across the range bins for a given Doppler frequency. To the authors' knowledge, this type of normalisation, which greatly improves CFAR performance, does not seem to be discussed in the open literature, although presumably some scheme is implemented in operational systems. The lack of discussion may simply be because measures of signal-to-interference ratio and ROC results are not affected by the PFA variation.

REFERENCES

[1]   Ward, K. D., Tough, R. J. A., and Watts, S.
       Sea clutter: Scattering, the K distribution and radar performance.
       *Waves in Random and Complex Media*, **17**, 2 (2007), 233–234.
       [Online]. Available:http://www.tandfonline.com/doi/abs/10.1080/17455030601097927.

[2]   Skolnik, M.
       *Introduction to Radar Systems* (3rd ed.). New York, NY: McGraw-Hill Science/Engineering/Math, Dec. 2002.

[3]   Gracheva, V., and Cerutti-Maori, D.
       First results of maritime MTI with PAMIR multichannel data.
       In *Proceedings of the International Conference on Radar*, Sept. 2013, 458–463.

[4]   Gracheva, V., and Cerutti-Maori, D.
       Multi-channel analysis of sea clutter for STAP applications.
       In *Proceedings of the 9th European Conference on Synthetic Aperture Radar*, Apr. 2012, 195–198.

[5]   McDonald, M., and Cerutti-Maori, D.
       An examination of the application of space time adaptive processing for the detection of maritime surface targets from high altitude airborne platforms.
       *Proceedings of the SPIE*, **8857** (2013), 705–710. [Online]. Available: http://dx.doi.org/10.1117/12.2026791.

[6]   McDonald, M., Cerutti-Maori, D., and Damini, A.
       Characterisation and cancellation of medium grazing angle sea clutter.
       In *Proceedings of the European Radar Conference (EuRAD)*, 2010, 172–175.

[7]   Gini, F., and Farina, A.
       Vector subspace detection in compound-Gaussian clutter. Part I: Survey and new results.
       *IEEE Transactions on Aerospace and Electronic Systems*, **38**, 4 (Oct. 2002), 1295–1311.

[8]   Cerutti-Maori, D., Klare, J., Brenner, A. R., and Ender, J. H. G.
       Wide area traffic monitoring with the SAR/GMTI system PAMIR.
       *IEEE Transactions on Geoscience and Remote Sensing*, **46**, 10 (Oct. 2008), 3019–3030.

[9]   Jakeman, E.
       On the statistics of K-distributed noise.

*Journal of Physics A: Mathematical and General*, **13**, 1 (1980), 31. [Online]. Available: http://stacks.iop.org/0305-4470/13/i=1/a=006.

[10] Watts, S., and Ward, K.
Spatial correlation in K-distributed sea clutter.
*IEE Proceedings, Part F: Communications, Radar and Signal Processing*, **134**, 6 (1987), 526–532.

[11] Zavorotny, V., and Voronovich, A.
Two-scale model and ocean radar Doppler spectra at moderate- and low-grazing angles.
*IEEE Transactions on Antennas and Propagation*, **46**, 1 (1998), 84–92.

[12] Plant, W. J., and Keller, W. C.
Evidence of Bragg scattering in microwave Doppler spectra of sea return.
*Journal of Geophysical Research: Oceans*, **95**, C9 (1990), 16,299–16,310. [Online]. Available: http://dx.doi.org/10.1029/JC095iC09pl6299.

[13] Walker, D.
Experimentally motivated model for low grazing angle radar Doppler spectra of the sea surface.
*IEE Proceedings: Radar, Sonar and Navigation*, **147** (2000), 3, 114–120.

[14] Walker, D.
Doppler modelling of radar sea clutter.
*IEE Proceedings: Radar, Sonar and Navigation*, **148**, 2 (Apr. 2001), 73–80.

[15] Lamont-Smith, T., Ward, K., and Walker, D.
A comparison of EM scattering results and radar sea clutter.
In *Proceedings of RADAR*, Oct. 2002, 439–443.

[16] Watts, S., Ward, K. D., and Tough, R. J. A.
The physics and modelling of discrete spikes in radar sea clutter.
In *Proceedings of the IEEE International Radar Conference*, May 2005, 72–77.

[17] Ward, K. D., and Tough, R. J.
Radar detection performance in sea clutter with discrete spikes.
In *Proceedings of the IEE International Radar Conference*, 2002.

[18] McDonald, M., and Cerutti-Maori, D.
Coherent radar processing in sea clutter environments part 2.
In press. *IEEE Transactions on Aerospace and Electronic Systems*.

[19] Ward, J.
Space–time adaptive processing for airborne radar.
In *IEE Colloquium on Space–Time Adaptive Processing (Ref. 1998/241)*, 1998, 2/1–2/6.

[20] Watts, S.
Radar detection prediction in K-distributed sea clutter and thermal noise.
*IEEE Transactions on Aerospace and Electronic Systems*, **AES-23**, 1 (1987), 40–45.

[21] Rosenberg, L., Watts, S., and Bocquet, S.
Application of the K + Rayleigh distribution to high grazing angle sea-clutter.

In *Proceedings of the International Radar Conference.*, Oct. 2014, 1–6.

[22] Ritchie, M., Woodbridge, K., and Stove, A.
Analysis of sea clutter distribution variation with Doppler using the compound K-distribution.
In *Proceedings of the IEEE Radar Conference*, May 2010, 495–499.

[23] Rosenberg, L.
Characterization of high grazing angle X-band sea-clutter Doppler spectra.
*IEEE Transactions on Aerospace and Electronic Systems*, **50**, 1 (Jan. 2014), 406–417.

[24] Sangston, K., and Gerlach, K.
Coherent detection of radar targets in a non-Gaussian background.
*IEEE Transactions on Aerospace and Electronic Systems*, **30**, 2 (1994), 330–340.

[25] Conte, E., De Maio, A., and Ricci, G.
Recursive estimation of the covariance matrix of a compound-Gaussian process and its application to adaptive CFAR detection.
*IEEE Transactions on Signal Processing*, **50**, 8 (2002), 1908–1915.

[26] Conte, E., and Longo, M.
Characterisation of radar clutter as a spherically invariant random process.
*IEE Proceedings, Part F: Communications, Radar and Signal Processing*, **134**, 2 (1987), 191–197.

[27] Reed, I., Mallett, J., and Brennan, L.
Rapid convergence rate in adaptive arrays.
*IEEE Transactions on Aerospace and Electronic Systems*, **AES-10**, 6 (1974), 853–863.

[28] Carlson, B. D.
Covariance matrix estimation errors and diagonal loading in adaptive arrays.
*IEEE Transactions on Aerospace Electronic Systems*, **24** (July 1988), 397–401.

[29] Roman, J., Davis, D., and Michels, J.
Multichannel parametric models for airborne phased array clutter.
In *Proceedings of the IEEE National Radar Conference*, May 1997, 72–77.

[30] Gierall, C. H., and Balaji, B.
Minimal sample support space–time adaptive processing with fast subspace techniques.
*IEE Proceedings: Radar, Sonar and Navigation*, **149**, 5 (Oct. 2002), 209–220.

[31] Conte, E., Lops, M., and Ricci, G.
Adaptive detection schemes in compound-Gaussian clutter.
*IEEE Transactions on Aerospace and Electronic Systems*, **34** (1998), 4, 1058–1069.

[32] Robey, F., Fuhrmann, D., Kelly, E., and Nitzberg, R.
A CFAR adaptive matched filter detector.
*IEEE Transactions on Aerospace and Electronic Systems*, **28**, 1 (1992), 208–216.

**Michael K. McDonald** received a B.Sc. (Hons.) degree in applied geophysics from Queens University in Kingston, Canada, in 1986 and a M.Sc. degree in electrical engineering in 1990, also from Queen's University. He received his Ph.D. degree in physics from the University of Western Ontario in London, Canada, in 1997. He was employed at ComDev in Cambridge, Canada, from 1989 through 1992 in the space science and satellite communications departments. He is a senior defence scientist in the Radar Systems and Exploitation section of Defence Research and Development Canada (DRDC), Ottawa, Canada, as well as an adjunct associate professor with the Department of Electrical and Computer Engineering at McMaster University. His research interests include the radar detection and tracking of maritime and land targets, nonlinear filtering for low observable targets, and multisensor fusion for enhanced detection and tracking. From 2012 through 2015, Dr. McDonald chaired the NATO SET 185 technical group on Maritime Radar Surface Surveillance Techniques and the High Grazing Angle Challenge.

**Delphine Cerutti-Maori** received an engineering degree from the Institut National des Sciences Appliquées de Lyon, Lyon, France, and a Ph.D. degree from the University of Siegen, Siegen, Germany, both in electrical engineering. Since 2000, she has been working at the FHR, Wachtberg, Germany, on various aspects of multidimensional signal processing for radar systems. From 2010 to 2015, she was leader of the Multi-Channel Signal Processing team in the Array Based Radar Imaging department. Since 2016, she has been leading the Space Reconnaissance team of the Radar for Space Observation department. From September 2008 to June 2009, she was guest scientist at DRDC. Her current research interests include both target detection and imaging with ground-based, airborne, and spaceborne (multichannel) radar and STAP.